ADVANCED ELECTRONIC MATERIALS
www.advelectronicmat.de

Large Exchange Bias, High Dielectric Constant, and Outstanding Ionic Conductivity in a Single-Phase Spin Glass

*Mohammad R. Ghazanfari, Archa Santhosh, Konrad Siemensmeyer, Friederike Fuß, Lennart Staab, Johannes C. Vrijmoed, Bertram Peters, Moritz Liesegang, Stefanie Dehnen, Oliver Oeckler, Paul Jerabek, and Günther Thiele**

The multigram synthesis of $K_2[Fe_3S_4]$ starting from K_2S and FeS is presented, and its electronic and magnetic properties are investigated. The title compound obtains a defect variant of the $K[Fe_2Se_2]$ structure type. Dielectric and impedance measurements indicate a dielectric constant of 1120 at 1 kHz and an outstanding ionic conductivity of 24.37 mS cm^{-1} at 295 K, which is in the range of the highest reported value for potential solid-state electrolytes for potassium-ion batteries. The Seebeck coefficient of the n-type conductor amounts to –60 µV K^{-1} at 973 K. The mismatch of the measured electrical resistivity and the predicted metal-like band structure by periodic quantum chemical calculations indicates Mott insulating behavior. Magnetometry demonstrates temperature-dependent, large exchange bias fields of 35 mT, as a consequence of the coexistence of spin glass and antiferromagnetic orderings due to the iron vacancies in the lattice. In addition, the decreasing training effects of 34% in the exchange bias are identified at temperatures lower than 20 K. These results demonstrate the critical role of iron vacancies in tuning the electronic and magnetic properties and a multifunctional material from abundant and accessible elements.

1. Introduction

The continuous increase in spintronic technology demand has been approached by a multitude of quantum materials as an interdisciplinary research line of chemistry, physics, and materials engineering.[1,2] Numerous scientific efforts have focused on designing new materials with the desired electronic and magnetic features by tuning the chemical composition, structural parameters, and physical modifications.[3,4] In recent years, defect variant structures have been considered as promising candidates to provide new, targeted properties and property combinations. The interdependence of magnetic and electronic structures to the partial vacancies on anion positions has been reported for a few ferrite and ferrate compounds indicating significant effects of vacancies on the Fermi level, orbital splitting, and geometrical interactions in the crystal structure, thereby changing the magnetization and the ionic conductivity.[5,6] The change in properties originates from the different vacancies of isolated cations and anions, as well as defects in the complex anionic motifs. For compounds including iron, depending on the structure, the iron vacancies can be considered either as vacancies of single cations, or as defects in the anionic motifs. Although the impact of iron

M. R. Ghazanfari, F. Fuß, G. Thiele
Fachbereich Biologie
Chemie
Pharmazie
Freie Universität Berlin
Fabeckstr. 34–36, 14195 Berlin, Germany
E-mail: guenther.thiele@fu-berlin.de

A. Santhosh, P. Jerabek
Institute of Hydrogen Technology
Helmholtz-Zentrum Hereon
Max-Planck-Straße 1, 21502 Geesthacht, Germany

The ORCID identification number(s) for the author(s) of this article can be found under https://doi.org/10.1002/aelm.202200483.

DOI: 10.1002/aelm.202200483

K. Siemensmeyer
Helmholtz-Zentrum Berlin für Materialien und Energie
Hahn-Meitner-Platz 1, 14109 Berlin, Germany

L. Staab, O. Oeckler
Fakultät für Chemie und Mineralogie
Universität Leipzig
Scharnhorststr. 20, 04275 Leipzig, Germany

J. C. Vrijmoed, M. Liesegang
Fachbereich Geowissenschaften
Freie Universität Berlin
Malteserstr. 74–100, 12249 Berlin, Germany

B. Peters, S. Dehnen
Fachbereich Chemie
Philips-Universität Marburg
Hans-Meerwein-Straße 4, 35032 Marburg, Germany

vacancies – in contrast to anion (mostly oxide) and other cation (e.g., alkali metals) vacancies – has been passed over in most reports, they could remarkably influence the materials' characteristics, in particular, the electronic and magnetic properties.

The magnetic exchange bias (EB) effect has attracted much interest as a critical characteristic of materials for upcoming spintronic applications, such as magnetic tunnel junctions, spin valves, high-density magnetic recording devices, and magnetic sensors.[7,8] Although the prototypical EB systems are conventionally defined for the interfaces of combined ferromagnetic (FM) and antiferromagnetic (AFM) bilayers,[9] there are a few artificial EB composites such as FM/spin glass,[10] ferrimagnetic/ferrimagnetic layers,[11] and core-shell nanocomposites and nanoparticles.[12] In all cases, the fundamental design is based on two different phases or doped compounds, such as metal/metal oxide, two different metal oxides, or metal alloys.[13] Despite many studies regarding EB systems during the last decades, only recently the pinning effect of defects at the FM/AFM interface was introduced as a dominant mechanism for the EB phenomenon.[14] The magnetic pinning effect is described as a barrier caused by different parameters of pinning agents that prevent the conventional motion of magnetic moments under an external magnetic field.[15] This interface could create a magnetic glassy area as a pinning agent of uncompensated moments,[16] which is in agreement with other reported systems exhibiting EB, including glassy orderings,[17], i.e., FM/spin glass and FM/spin ice.[18,19] Recently, Maniv et al.[20] introduced a new EB system consisting of a AFM/spin-glass combination in a Fe_xNbS_2 bulk system which revealed the captious effects of iron vacancies. Spin glass phases are magnetic phases with metastable ground states that differ from FM and AFM orderings.[21–23] Spin glass phases introduce magnetic domains with short-range disorder within a long-range ordering of parallel and/or antiparallel ordered magnetic moments, providing a metastable magnetic structure similar to mixed FM/AFM ordering.[21–23] Such magnetic behavior is discussed to be caused by defects in the crystal structure, uncompensated magnetic moments, and geometrical frustration, resulting from the competition between the orientation of magnetic moments due to the constrains in magnetic sites.[24,25]

In parallel to the magnetic characteristics, electrical properties of materials strongly depend on the chemical composition and the crystal structure. Slight alterations can lead to decisive changes in electrical parameters such as the capacity, resistivity, and both electronic and ionic conductivities. Although alkali metal-ion batteries such as lithium-, sodium-, and potassium-ion batteries are the flagship of modern energy storage, they are faced with several challenges, in particular regarding common liquid electrolyte. State-of-the-art liquid or composite electrolytes are inherently prone to safety issues related to the flammability, leakage of liquid electrolytes, undesired reactions between electrodes and electrolytes, complicated connections between components, and the assembling of the cells.[26] Solid-state electrolytes are considered the safest candidates to replace commercial liquid electrolytes. By using solid-state electrolytes, the assembly of the battery cells have less costs and difficulties.[27] Several solid-state electrolytes have been introduced to prevail over the mentioned challenges.[27] Ionic conductivity is a key criterion for solid-state electrolytes which is required to be high enough at ambient temperatures in order to provide sufficient alkali metal-ion mobility.[28] Despite the numerous investigations on conductive materials, almost all of them indicate comparably low ionic conductivities in the range of 10^{-8} to 10^{-4} S cm^{-1}, which is not comparable to commercial liquid electrolytes.[26]

This study focuses on sulfido ferrates, i.e., salts comprising $[Fe_xS_y]^{q-}$ (poly)anionic units. The inherent advantages of these materials are the combination of abundant and nontoxic elements that are accessible through socially and environmentally controlled mining process. A few sulfido ferrates such as $K[FeS_2]$, $K[Fe_2S_3]$ and $K_3[Fe_2S_4]$ are known in the literature,[29,30] but have never been examined for their electric and magnetic performance. In the course of our studies, we obtained $K_2[Fe_3S_4]$ (**1**) as a novel representative in the K–Fe–S ternary system which is the first potassium sulfido ferrate including iron solely in the oxidation state +II. Extensive analysis focused on the origins of the electronic and magnetic behaviors of **1** such as magnetic exchange bias and spin glass behavior as well as ionic conductivity, dielectric properties, and thermoelectric properties with regard to the characteristics of the crystal structure is presented. This combination of analyses shall give a comprehensive understanding of the material's characteristics and facilitate potential applications, such as the utilization as a solid-state electrolyte. To the best of our knowledge, there is no report on either the exchange bias and spin glass behavior, nor on observations of dielectric properties and ionic conductivity in sulfido ferrate salts with potential for a solid-state electrolyte in potassium-ion batteries.

2. Results and Discussion

The reaction of K_2S with three equivalents of FeS in a silica glass ampoule at approx. 1250 K for 15 min yields pure **1** without the need for further purification, according to the equation presented in **Scheme 1**. The obtained amount of **1** is only limited by the volume of the ampoule, typically yielding ≈50 g per batch.

The compound crystallizes in the space group type *I*4/mmm with one formula units in the unit cell with $a = 3.7726(2)$ Å, $c = 13.3510(9)$ Å, $V = 190.02(2)$ Å^3. The iron atoms are tetrahedrally coordinated by sulfur atoms with Fe–S bond lengths of 2.344(8) Å. Full information about the atom positions and bond lengths are available in the supporting information (SI). Edge-sharing $[Fe^{II}S_4]$ tetrahedra form anionic layers in the (001) plane (**Figure 1**), which can be considered as an anionic substructure of **1**. The structure is a defect variant of the $K[Fe_2Se_2]$ structure type[22] with the iron positions statistically occupied at 75%, which was confirmed by quantitative energy-dispersive X-ray spectroscopy, EDX (Figure S1, Supporting Information). Rietveld structure refinement based on powder diffraction data (Figure S2, Supporting Information) confirms the formation of a high-purity

$$K_2S + 3\ FeS \xrightarrow[\approx 15\ min]{\approx 1250\ K} K_2[Fe_3S_4]$$

Scheme 1. Reaction equation for the synthesis of **1**.

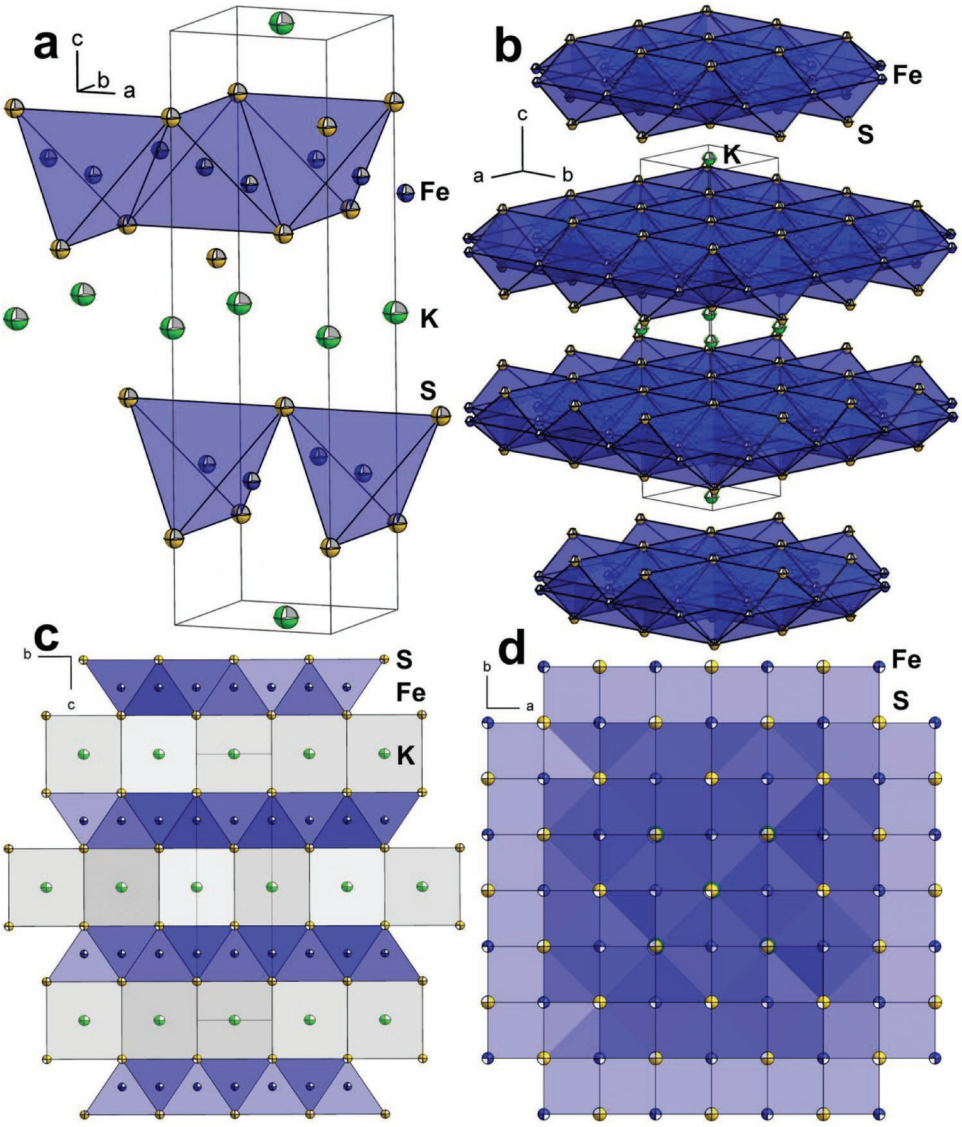

Figure 1. Excerpt from the crystal structure of **1**. The iron vacancies (25%) are omitted. a) Edge-sharing $[Fe^{II}S_4]$ tetrahedra in the *ab* plane (in blue), including separately depicted tetrahedra in the lower row and edge-shared tetrahedra depicted in the upper row. b,d) Edge-sharing tetrahedra forming a 2D anionic substructure of $[Fe_3S_4]^{2-}$ as a layer in the *ab* plane. c) Layered sublattice of Fe-S tetrahedra and cubic environment of potassium ions in the *ab* plane. Selected bond lengths (Å) and angles (°): Fe–S: 2.344(8), K–S: 3.302(8), S–Fe–S: 107.144(2)-110.647(2).

and strain-free single-phase material with a degree of crystallinity of 92.5% and an average crystallite size of 616 nm ± 3%.

1 is isotypic to some selenido and tellurido ferrates, such as $K[Fe_{1.5}Se_2]$, $K[Fe_{1.5}Te_2]$, and $K_x[Fe_{2-y}Se_2]$.[23,24] Magnetic structures, as well as the impact of the iron vacancies on the magnetic ordering have been reported for $K[Fe_{1.5}Se_2]$, $K[Fe_{1.5}Te_2]$, and $K_x[Fe_{2-y}Se_2]$.[23,24] The AFM structure of $K_x[Fe_{2-y}Se_2]$ phases was previously confirmed using neutron diffraction by Zhao et al.[32] Moreover, the reported quantum chemical calculations revealed that in isotypic structures such as $Tl_2[Fe_3Se_4]$, $K_2[Fe_3Se_4]$, $Rb_2[Fe_3Se_4]$, and $Cs_2[Fe_3Se_4]$ the iron vacancies form a rhombus-like ordering along the layers of the anionic substructure.[31,32]

To determine the magnetic structure of **1**, the magnetic ordering can be determined by the shape and trend of the magnetization-field (M-H) curves. Field-dependent magnetometry of **1** at constant temperatures (Supplementary Figure S3 and S4) indicates narrow non-linear hysteresis loops. The observed hysteresis loop in the range of low fields (–0.50–0.50 T) is a sign of FM ordering while the unsaturated linear part in the range of higher fields (1.00–5.00 T) is one of the preliminary characteristics of AFM structures.[33] This combination suggests a complex magnetic structure in **1** with a coexistence of both ordering types. For the parent $K[Fe_2Se_2]$ structure, only long-range AFM ordering is reported.[22]

The complex behavior in the field-dependent magnetization curves of **1** can be explained by the partial short-range disorder in the AFM structure.[34] Regarding the statistical iron occupancy of 75% of the magnetic iron ions, these vacancies can partially disrupt the long-range magnetic order and cause

locally frustrated magnetic moments, creating magnetic disordered areas. Such magnetically frustrated and disordered areas are referred to as metastable spin-glass structures.[34] Indeed, the iron vacancies in **1** can be considered to create a spin glass structure which causes a short-range ferrimagnetic ordering combined with an AFM long-range ordering.

In addition, temperature-dependent magnetization curves at constant fields and after cooling under zero applied field, which are denoted field cooled (FC) and zero field cooled (ZFC) curves, respectively, provide more information about the magnetic ordering. **Figure 2**a depicts the FC/ZFC curves of **1** in the temperature range of 1–380 K. The FC and ZFC curves are separated over the whole temperature range and particularly at low temperatures, which indicates the existence of a spin glass structure.[34] The difference of the magnetization values between FC and ZFC curves decreases with temperature in the range of 2–20 K. At higher temperatures, the difference gradually decreases as a function of temperature. To clearly identify the characteristics of both AFM and spin glass ordering, the tendency of the variation can be followed by the first derivative of the magnetization difference, $d[M_{FC} - M_{ZFC}]/dT$, where M_{FC} and M_{ZFC} are the magnetization values of the FC and the ZFC curves, respectively. The minimum value of the first derivative (Figure 2a) describes the magnetic freezing temperature at around 20 K, which corresponds to the changepoint of the ZFC curve.[35,36]

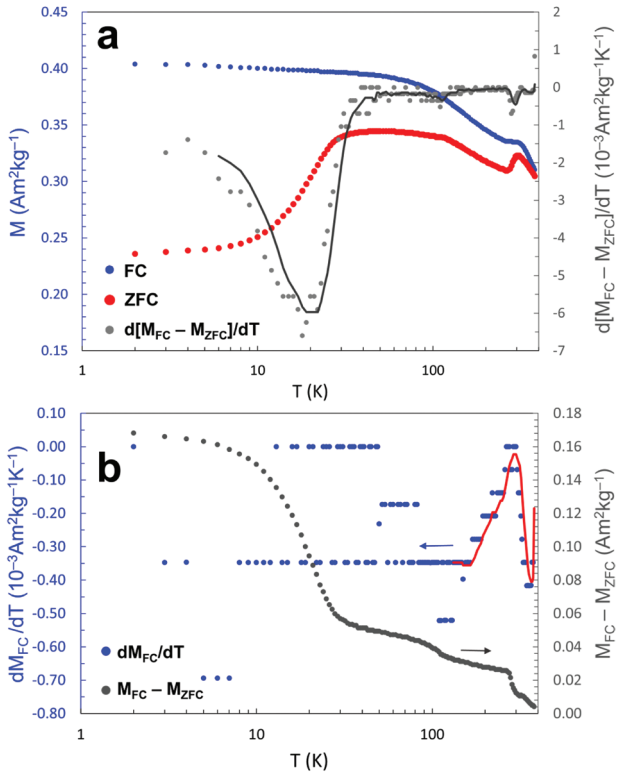

Figure 2. Temperature-dependent magnetization curves. a) Left axis: FC and ZFC curves under an applied field of 5 mT. Blue: FC, Red: ZFC. Right axis: $d[M_{FC}\text{-}M_{ZFC}]/dT$ as a function of increasing temperature. Gray dots: calculated values, Gray line: fitted trendline. The minimum at around 20 K indicates the freezing temperature of the spin-glass phase. b) Left axis: dM_{FC}/dT as a function of the temperature. Blue: calculated values, Red: fitted trendline. The local maximum at around 314 K indicates the Néel temperature of the AFM phase. Right axis M_{FC}-M_{ZFC} variation as a function of the temperature (gray dots). The extrapolated intercept with the *x*-axis shows that the bifurcation temperature (irreversibility) is higher than the accessible experimental temperature range (>380 K).

At temperatures around 314 K there is a small cusp in both the FC and the ZFC curves which corresponds to the Néel temperature of the AFM phase.[36] Above the Néel temperature, the dominant magnetic structure is transformed from an AFM to a paramagnetic ordering. In addition, the values for the ZFC inverse susceptibility (χ^{-1}) indicate a significant deviation from the fitting line of the Curie-Weiss law at around 314 K (see SI), validating the Néel temperature determination of the AFM phase.[23] The negligible change in slope of the FC curve at temperatures slightly below the freezing temperature can be considered as additional confirmation of the spin-glass effects. To confirm the AFM ordering and Néel temperature, the magnetization variation of the FC curve can be investigated with means of the derivation equation dM_{FC}/dT.[35,36] The maximum value of the derivative dM_{FC}/dT (Figure 2b) demonstrates the same Néel temperature of 314 K. The bifurcation temperature which is defined as a starting point of the separation between the values for FC and ZFC, indicates a reversible character of the magnetic behavior.[36] The (bifurcation) temperature of irreversibility of the structure is calculated to be above 380 K, the maximum available measurement range, with the following temperature-dependent equation.

$$\Delta M(T) = M_{FC} - M_{ZFC} \tag{1}$$

A detailed analysis of the field-magnetization curve at 3 K (Supplementary Figure S4, Supporting Information) displays asymmetric hysteresis loops including shifts in both remanence and coercivity. Under the applied magnetic fields, the shifts are observed in opposite directions. Such asymmetries are a well-known sign of exchange bias effects that shift the hysteresis loop horizontally and vertically.[7,10] To investigate the induced EB field more precisely, the FC hysteresis loops were measured at different temperatures after cooling under an applied field of 3.00 T (**Figure 3**a), confirming the significant shifting trends for both the remanence and coercivity values at low temperatures of 3–20 K. Figure 3b shows the variations of the EB field, which is equivalent to shifts in the coercivity and the remanence as a function of increasing temperature. At temperatures above 100 K, both the EB field and the remanence dramatically decrease to negligible values and finally reach a plateau around 1 mT for temperatures beyond 200 K. Such behavior is in good agreement with the calculated freezing temperature of the spin-glass phase based on the FC/ZFC curves.

At 3 K, a large EB field and EB remanence of 35 mT and 0.27 Am^2 kg^{-1}, respectively, are observed (Figure 3c). The disordered spin-glass moments can interact with antiferromagnetically ordered moments and pin them to induce the EB behavior.[20] Indeed, the iron vacancies could play a mechanistic role in providing spontaneous EB effects by pinning the ordered magnetic areas. These findings confirm the effects of the iron vacancies on the recently introduced EB field in the AFM/spin-glass combined ordering.[20,21]

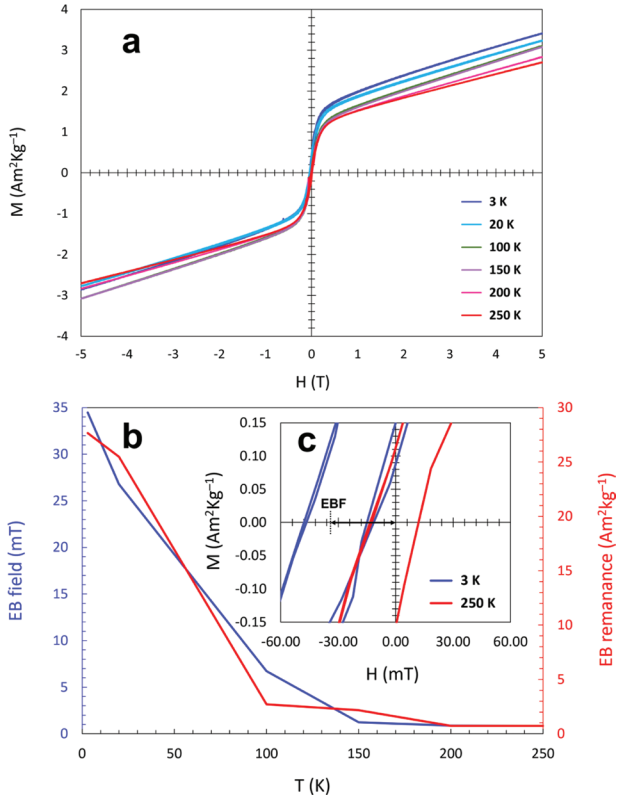

Figure 3. Magnetization curves after cooling under an applied field of 3.00 T. a) M-H hysteresis curves at different temperatures using an applied field of up to 5.00 T. b) Left axis: Variations of EB field. Right axis: EB remanence as a function of increased temperature. c) Enlarged view of M-H curves at temperatures of 3 and 250 K displaying an exchange bias field of 35 mT at 3 K.

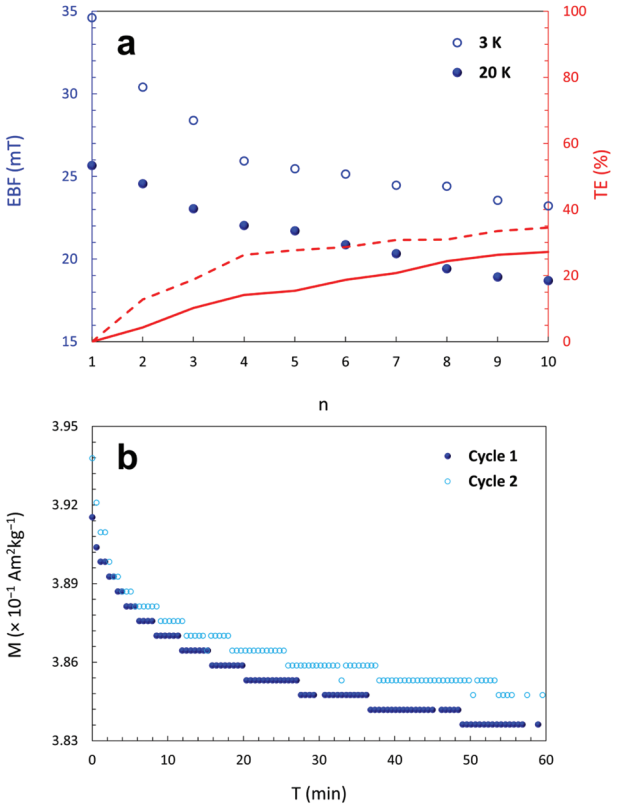

Figure 4. a) Cyclic hysteresis magnetization measurements at 3 and 20 K after cooling under an applied field of 3.00 T. *n* is the cycle number. Left axis: Variation curves of EB field (EBF) as a function of the hysteresis cycle *n*. Right axis: Variation curves of the training effect as a function of the hysteresis cycle n. b) Thermoremanent magnetization measurements for the first two hysteresis cycles at 3 K after cooling under an applied field of 3.00 T.

Furthermore, the cyclic hysteresis loops at temperatures of 3 and 20 K (**Figure 4**) demonstrate the decreasing training effects (TE) of around 34% calculated with Equation 2.[35]

$$TE = 100 - \left[\left(1 - \left[(EB_1 - EB_n)\cdot EB_1^{-1}\right]\right)\times 100\right]\% \quad (2)$$

EB_1 and EB_n are the measured exchange bias fields for the first and n^{th} cycles, respectively. The observed training effect can be related to multiple easy axes, as possible directions for the reorientation of the magnetic moments in the high symmetry AFM phase which lead to a decrease of the coercivity,[22] as well as the existence of the spin-glass phase.[35–37] The metastable pinned spin-glass moments reorient during the reversal of the field, but after changing the field back to the previous direction, the moments cannot reconfigure in the same alignment.[34] Indeed, the moments of the spin-glass domain start to gradually defreeze during the cyclic field reversals.[35] The EB field decreases from ≈35 to 23 mT at 3 K and from 26 to ≈18 mT at 20 K during ten continuous cycles of the hysteresis loops. The reduced rate of decreasing the EB field could be explained by an easier realignment of the spin-glass moments into the original directions at higher temperatures due to thermal agitation. In addition, the thermoremanent magnetization measurements for the first two hysteresis cycles were carried out at 3 K after cooling the sample under an applied field of 3.00 T, which indicate the simultaneous effects of temperature and cyclic measurements on the magnetization and relaxation values. The magnetic relaxation behavior was recorded after the removal of the applied field and can be attributed to the spin-glass phase.[20] A slight difference in the thermoremanent magnetization within the second cycle is in line with the trend of the training effects.

The iron vacancies in **1** further impact the electronic structure and the corresponding properties, including semiconductivity, electrical resistivity, thermal conductivity, and dielectric features, which allows the utilization of **1** as a multipurpose material.[35–37] In order to determine the electrical properties of the sulfido ferrate, we examined the dielectric and thermoelectric behavior of **1**.

The dielectric properties of pellets of **1** sintered at 1100 K were measured at room temperature as a function of an alternating current, AC, with electrical field frequencies in the range of 0.10–100 kHz. The real part ε' of the electrical permittivity can provide the dielectric constant κ. The electrical permittivity was calculated using the measured capacitance C, the surface of the electrode plates A, the distance between the electrode plates d, and the permittivity of vacuum (ε_0: 8.85×10^{-12} m^{-3} kg^{-1} s^4 A^2) according to Equation 3.[24]

$$\varepsilon = C \cdot d \cdot \varepsilon_0^{-1} \cdot A^{-1} \quad (3)$$

Figure 5a shows the variations of the dielectric constant and dielectric loss of **1** as a function of the frequency. At increasing frequency, both dielectric constant and dielectric loss rapidly decreases due to the pining of charge domains and the vanishing of the space charge polarization mechanism.[24] Grain boundaries, disordering and displacements in the grains, vacancies, and other defects could act as significant pinning agents. The unexpected slight increase in dielectric constant at frequencies between 0.40 and 0.80 kHz might be caused by fringe effects.[38] Although the space charge polarization mechanism loses effect at high frequencies, the vacancies still work as charge carriers and defects dipoles which are polarizable up to the MHz frequency range.[39,40] Figure 5b depicts the

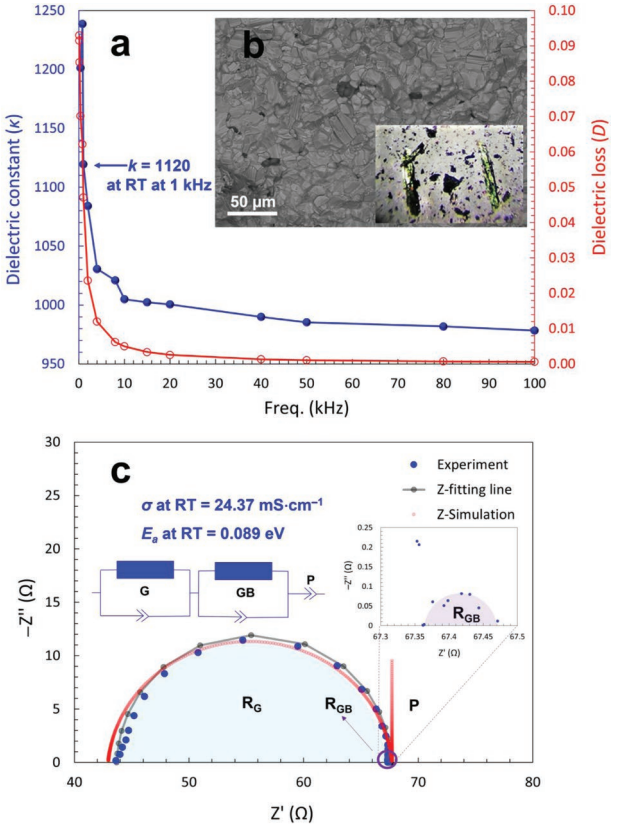

Figure 5. a) Dielectric constant κ and dielectric loss of a pellet of **1** sintered at 1100 K as a function of the frequency of the AC electrical field. b) Main frame: High resolution backscattered electron image obtained with a Zeiss Sigma 300VP FE-SEM with beam energy of 20 kV displaying the grains and grain boundaries on the cross-section surface of the sintered pellet of **1**. Inset: Optical microscopy photograph of the obtained single crystals of **1** covered by Paratone oil at 30x magnification. c) Nyquist plot of the complex impedance of a pellet of **1** sintered at 1100 K including two semicircular arcs for the ordered (G) and disordered (GB) areas as well as the polarization (P) of the electrode (main frame). Inset: Experimental data for $67.3 < Z' < 67.5$ indicates a small semicircular arc for the GB areas. Blue: Experimental data. Gray: fitted line with the averaged points to experimental data. Red: Simulated plot using an equivalent circuit with two parallel series of resistance and CPE for ordered and disordered areas (left inset). CPE is the constant phase element as a frequency-independent capacitor.

scanning electron microscopy micrograph obtained with the high resolution backscattered electron detector displaying the grains and grain boundaries of the cross-section surface on the sintered pellet of **1**.

The measured κ at 1 kHz is 1120 ± 1% (average value of three measurements) while the dielectric loss is around 0.025, which is comparable to the κ value for barium titanates (1000 – 1200), a well-known commercial capacitor, and larger than many other dielectric materials, such as strontium titanate, barium strontium titanate, and zirconate titanate.[41] In addition, most of the ceramic-based dielectrics require higher sintering temperatures, commonly ≥1300 K, to achieve such dielectric constants.[39,42]

The complex impedance measurements were employed to investigate the electrical conductivity of **1**. The disordered areas including grain boundaries and other structural defects can act as efficient polarization areas in the material. These effects were analyzed by means of a Nyquist plot according to the equivalent circuit model with two parallel resistor-constant phase element series for ordered and disordered areas (Figure 5c). The plot displays two semicircular arcs with a small overlap which can be assigned to ordered and disordered areas, respectively. This combination agrees with the model of grain-grain boundaries for solid-state electrolytes in Li/Na-ion batteries.[43] Besides the semicircular arcs, there is a linear spike at low frequencies, which is related to the polarization of the electrode. This indicates an ionic contribution to the electrical conductivity.

The ionic conductivity and activation energy of **1** was calculated with the Nyquist and Arrhenius equations, yielding values of 24.37 mS cm^{-1} and 0.089 eV, respectively. The activation energy measurement was conducted by the DC polarization method. The number of charge carriers were approximated and divided to the two categories of electronic conductivity and ionic conductivity. The dominant transferring contribution is the ionic conductivity, which is explainable with the role of potassium ions as the charge carriers in the vacancy-included crystal structures of **1**. This calculated ionic conductivity (details provided in the SI) for **1** is decisively higher than for common materials discussed as solid-state electrolytes and is comparable to prevalent liquid electrolytes.[26-2-8] To the best of our knowledge, this is the highest reported conductivity of potassium ions with potential for an application as a solid-state electrolyte in potassium-ion batteries, only second to $K_2[Fe_4O_7]$, which comprises open conductivity channels.[44]

For most solid-state electrolytes, structural defects involve lithium or sodium vacancies that improve the ionic conductivity.[45] However, the role of vacancies within (poly-)anionic substructures remains largely undiscussed. Due to the layered anionic substructure of **1**, rhomboid-like distributed iron vacancies[31,32] (**Figure 6**a) can be considered as one of the possible vacancy distributions, which directly impacts the energy of the K–K interactions between the potassium layers, thereby changing the probability of ion mobility along these channels, similar to the well-known effects of anionic defects.[5,6] However, structural relaxations originating from induced stress around the iron vacancies can act as a conductivity barrier.[46] In addition, iron vacancies within the anionic layers provide hidden channels of diffusion perpendicular to the potassium layers (Figure 6b). A similar role of iron vacancies has been

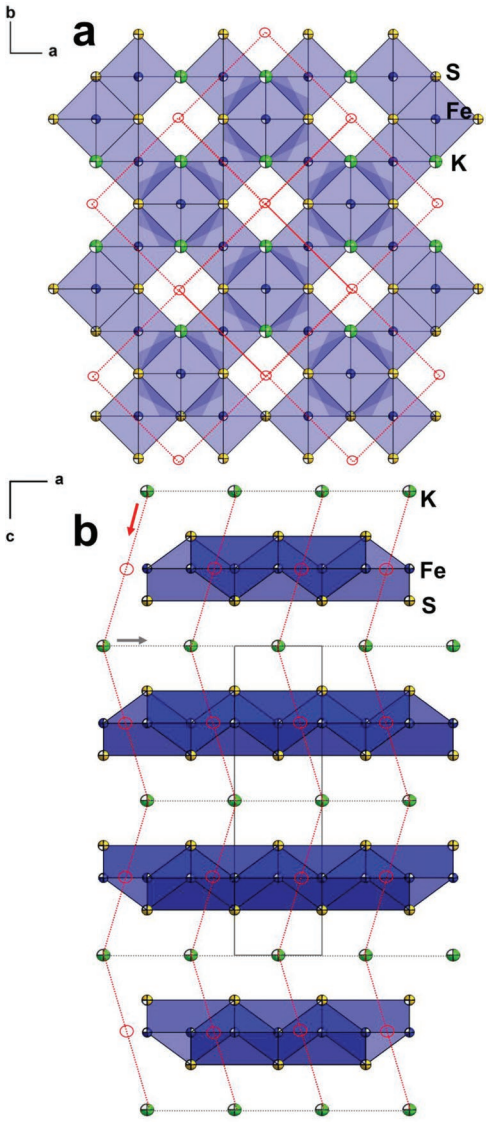

Figure 6. Excerpt of the crystal structure of **1** a) Display of one of the possible distributions of the crystal vacancies, dotted lines: rhomboid-like motif. b) Two potential conductivity channels. Gray dotted lines: Linear channel between anionic layers. Red: Zigzag channel through the anionic layers.

introduced into computational simulations, leading to cross-linking between two perpendicular channels of sodium-ions in $Na_{2+\delta}$ $Fe_{2-\delta/2}$ $(SO_4)_3$.[46] In **1**, the iron vacancies create a new channel linked in a zigzag manner that contributes to the ionic conductivity and reduces the activation energy. Moreover, the free electron charges, which are statistically distributed, could be trapped within the disordered areas with vacancies and grain boundaries as the polarization centers. The accumulated charges could undergo charge-hopping[47] as a minor mechanism to increase the total electrical conductivity, although the mechanism and impact of charge accumulation on the transfer of charges is still not fully understood.

As the statistical occupation of the iron atoms could lead to a low thermal conductivity of **1**, thermoelectric properties were investigated. The thermal conductivity lies around 0.6 Wm^{-1} K^{-1} at room temperature and decreases to approx. 0.5 Wm^{-1} K^{-1} at 973 K. However, with electrical conductivities ranging from 3 S cm^{-1} at room temperature to 32 S cm^{-1} at 973 K, these values are orders of magnitude too low for a promising thermoelectric figure of merit (zT). A maximum zT of 0.024 is obtained at 973 K,[48,49] which is also caused by comparably low absolute Seebeck coefficients between −30 and −60 mμV K^{-1}. Full details on the thermoelectric properties of **1** are provided in the SI.

In contrast to conventional insulating dielectric materials with wide electronic band gaps, new-generation dielectrics with band gaps in the range of semiconductors could act as both the dielectric and the semiconductor in microelectronic applications.[50] As the dark green color of the compound contradicts the expected bandgap according to the concept of dimensional reduction,[51] we performed UV-visible measurements. The optical band gap of **1** was determined from Tauc plots (Figures S13 and S14, Supporting Information). The indirect band gap is 1.34 eV, with an additional direct transition at 1.35 eV. At first, the experimental data stood in contrast to the results from our quantum chemical calculations: Band structure and electron density of states in both, partial elemental density of states (PDOS) and total density of states (TDOS), of **1** were simulated by means of periodic density functional theory (DFT) calculations (for computational details see SI). Our initial DFT calculations (according to functions of BPE) utilizing various GGA functionals predicted a metal-like behavior with a band gap of zero. Although this was in agreement with other reported DFT simulations of isotypic structures, e.g. $K[Fe_{1.5}Se_2]$, $K_x[Fe_{2-y}Se_2]$, and Tl $[Fe_{1.5}Se_2]$,[31,32] it clearly disagreed with our experimental observations. However, employing the more advanced semilocal meta-GGA functional SCAN,[52] which in many cases matches or even surpasses the accuracy of computationally very expensive hybrid functionals,[53] enabled us to calculate the narrow band gap of **1**. The calculated valence band maximum (VBM) and the conduction band minimum (CBM) lie at 2.969 eV and 3.284 eV, respectively, giving a direct band gap of 0.314 eV at the Γ-point (**Figure 7**). The TDOS is completely symmetrical as expected from the AFM nature of the material. The DOS plot illustrates Fe(*3d*) and S(*p*) hybridized states as well as valence bands as the major contributors toward the conductivity. Partial and orbital-resolved DOS plots and further information on the calculated parameters are available in the SI. A metal-like band structure and DOS are reported for several structurally related compounds such as $K[Fe_2Se_2]$ and $K[Fe_2S_2]$ by means of quantum chemical calculations.[54,55] To the best of our knowledge this is the first example of a non-zero band gap of isotypic structures of sulfido metalates correctly predicted with first-principle calculations.

The seeming contradiction between the calculated metal-like band gap in our initial DFT calculations and the experimentally determined electrical resistivity can be attributed to Mott insulating behavior stemming from strong interelectronic repulsion within the partially filled *d* shells[56] that is not properly described utilizing conventional GGA functionals without Hubbard U correction.[57] This, however, can be overcome by employing a density functional like SCAN that is able to better rectify the DFT self-interaction errors.[58] Although Mott insulation in chalcogenido metalates was initially introduced for

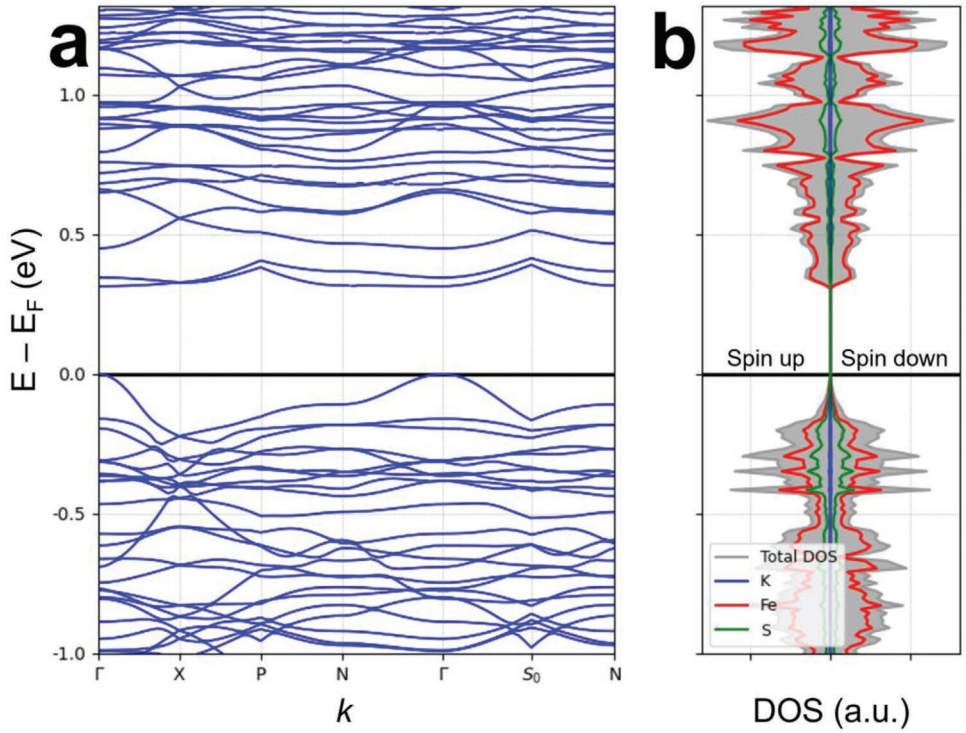

Figure 7. a) Calculated electronic band structure of **1** utilizing the SCAN functional. *k* is the wavevector. The valence band maximum is shifted to zero on the energy scale. b) The total and partial DOS indicate symmetric contributions of spin- up and spin-down electrons.

cuprates,[59] there are a few theoretical predictions on the Mott insulating behavior in the related sulfido and selenido ferrates such as $Rb_{1-x}[Fe_{1.5-y}S_2]$, $K_x[Fe_ySe_2]$, and $Tl_x[Fe_ySe_2]$. Furthermore, for a couple of AFM ferrates with iron vacancies, Mott insulating behavior has been reported in conjunction with superconductivity.[60]

3. Conclusion

In conclusion, the multigram synthesis of hitherto unreported $K_2[Fe_3S_4]$ as a defect variant of the $K[Fe_2Se_2]$ family using an uncomplicated and rapid procedure was presented. **1** is the first potassium sulfido ferrate (II) salt and exhibits a significant exchange bias field and a remanence of 35 mT and 0.27 $Am^2\ kg^{-1}$, respectively. The observed exchange bias effects can be explained by the newly introduced mechanism of the coexistence of AFM and spin glass structures.[20] The statistical iron vacancies of 25% in the structure are discussed to play a critical role in the magnetic frustration and formation of the spin-glass phase. **1** shows distinguished dielectric behavior with high κ values (1120 ± 1% at 1 kHz) comparable to the well-known commercial barium and strontium titanates. The pinning effects of vacancies in the electrical polarization areas lead to large and stable κ values, even at higher frequencies. The outstanding ionic conductivity of 24.37 mS cm^{-1} with a low activation energy of 0.089 eV is the second highest reported value for potential potassium-based solid-state electrolytes, which could originate from the iron vacancies introducing conductivity channels perpendicular to the potassium layers as pathways for potassium ion transfer. **1** was shown to have an indirect optical band gap of 1.34 eV in the range of semiconductors as well as Mott insulating behavior which is implied by the results of DFT calculations utilizing different density functional classes. Due to the combination of outstanding ionic conductivity, high dielectric values, and spin glassy magnetic properties, $K_2[Fe_3S_4]$ represents a multifunctional material with a non-toxic, abundant element combination.

4. Experimental Section

All materials, synthetic methods, characterization techniques, and full data of measurements are given in the supporting information.

Supporting Information

Supporting Information is available from the Wiley Online Library or from the author.

Acknowledgements

The authors thank the Verband der Chemischen Industrie e.V. for a Liebig scholarship, the Volkswagen Stiftung within the framework of an "Experiment!" funding, the German-American Fulbright Commission for a Fulbright-Cottrell Award, the Hans-Böckler-Stiftung for a scholarship for doctoral candidates. The authors acknowledge the North-German Supercomputing Alliance (HLRN) for providing High-Performance Computing (HPC) resources. Core facility BioSupraMol (supported by DFG) is acknowledged for X-Ray diffraction time. The authors thank Clara A. von Randow for the fruitful suggestions on the manuscript as

well as Dr. Karel Prokes and the Quantum Materials Core Lab facilities at Helmholtz Zentrum Berlin (HZB) for the magnetic measurements.

Open access funding enabled and organized by Projekt DEAL.

Conflict of Interest

The authors declare no conflict of interest.

Data Availability Statement

The data that support the findings of this study are openly available in ICSD at https://icsd.fiz-karlsruhe.de/search/basic.xhtml, reference number 2159680.

Keywords

dielectric, frustrated magnetism, iron vacancy, metalate, Mott insulators, solid-state electrolytes, transport properties

Received: April 28, 2022
Revised: June 22, 2022
Published online:

[1] C. Ahn, A. Cavalleri, A. Georges, S. Ismail-Beigi, A. J. Millis, J. M. Triscone, *Nat. Mater.* **2021**, *20*, 1462.
[2] B. Huang, M. A. McGuire, A. F. May, D. Xiao, P. Jarillo-Herrero, X. Xu, *Nat. Mater.* **2020**, *19*, 1276.
[3] N. A. Spaldin, R. Ramesh, *Nat. Mater.* **2019**, *18*, 203.
[4] N. Samarth, *Nat. Mater.* **2017**, *16*, 1068.
[5] Y. H. Hou, X. Chen, X. L. Guo, W. Li, Y. L. Huang, X. M. Tao, *J. Magn. Magn. Mater.* **2021**, *538*, 168257.
[6] T. Das, J. D. Nicholas, Y. Qi, *J. Mater. Chem. A* **2017**, *5*, 4493.
[7] F. Radu, H. Zabel, In: (Eds: H. Zabel, S.D. Bader) *Springer Tracts in Modern Physics*, Vol. *227*. Springer, Berlin, Heidelberg **2008**.
[8] W. H. Meiklejohn, C. P. Bean, *Phys. Rev.* **1957**, *105*, 904.
[9] G. R. Haripriya, C. M. N. Kumar, R. Pradheesh, L. M. Martinez, C. L. Saiz, S. R. Singamaneni, T. Chatterji, V. Sankaranarayanan, K. Sethupathi, B. Kiefer, H. S. Nair, *Phys. Rev. B* **2019**, *99*, 184411.
[10] M. Ali, P. Adie, C. H. Marrows, D. Greig, B. J. Hickey, R. L. Stamps, *Nat. Mater.* **2007**, *6*, 70.
[11] F. Radu, R. Abrudan, I. Radu, D. Schmitz, H. Zabel, *Nat. Commun.* **2012**, *3*, 715.
[12] J. A. Gonzalez, J. P. Andres, R. L. Anton, J. A. De Toro, P. S. Normile, P. Muniz, M. Riveiro, J. Nogues, *Chem. Mater.* **2017**, *29*, 5200.
[13] Y. Guo, L. Shi, S. Zhou, J. Zhao, C. Wang, W. Liu, S. Wei, *J. Phys. D: Appl. Phys.* **2013**, *46*, 175302.
[14] H. Ohldag, A. Scholl, F. Nolting, E. Arenholz, S. Maat, A. T. Young, M. Carey, J. Stöhr, *Phys. Rev. Lett.* **2003**, *91*, 017203.
[15] Q. C. Sun, T. Song, E. Anderson, E. Brunner, J. Förster, T. Shalomayeva, T. Taniguchi, K. Watanabe, J. Gräfe, R. Stöhr, X. Xu, J. Wrachtrup, *Nat. Commun.* **2021**, *12*, 1989.
[16] I. K. Schuller, R. Morales, X. Batlle, U. Nowak, G. Güntherodt, *J. Magn. Magn. Mater.* **2016**, *416*, 2.
[17] M. Kiwi, *J. Magn. Magn. Mater.* **2001**, *234*, 584.
[18] T. C. Schulthess, W. H. Butler, *Phys. Rev. Lett.* **1998**, *81*, 4516.
[19] V. M. Parakkat, K. Xie, K. M. Krishnan, *Phys. Rev. B* **2019**, *99*, 054429.
[20] E. Maniv, R. A. Murphy, S. C. Haley, S. Doyle, C. John, A. Maniv, S. K. Ramakrishna, Y. L. Tang, P. Ercius, R. Ramesh, A. P. Reyes, J. R. long, J. G. Analytis, *Nat. Phys.* **2021**, *17*, 525.
[21] M. Lee, *Nat. Phys.* **2021**, *17*, 434.
[22] W. Li, H. Ding, Z. Li, P. Deng, K. Chang, K. He, S. Ji, L. Wang, X. Ma, J. P. Hu, X. chen, Q. K. Xue, *Phys. Rev. Lett.* **2012**, *109*, 057003.
[23] S. K. Panda, I. Dasgupta, T. Saha-Dasgupta, *Phys. Rev. B* **2015**, *92*, 104421.
[24] W. Bao, G. N. Li, Q. Z. Huang, G. F. Chen, J. B. He, D. M. Wang, M. A. Green, Y. M. Qiu, J. L. Luo, M. M. Wu, *Chin. Phys. Lett.* **2013**, *30*, 027402.
[25] J. E. Greedan, *J. Mater. Chem.* **2001**, *11*, 37.
[26] M. Zhou, P. Bai, X. Ji, J. Yang, C. Wang, Y. Xu, *Adv. Mater.* **2021**, *33*, 2003741.
[27] Y. Liu, C. Gao, L. Dai, Q. Deng, L. Wang, J. Luo, S. Liu, N. Hu, *Small* **2020**, *16*, 2004096.
[28] H. Yuan, H. Li, T. Zhang, G. Li, T. He, F. Du, S. Feng, *J. Mater. Chem. A* **2018**, *6*, 8413.
[29] I. Han, Z. Jiang, C. dela Cruz, H. Zhang, H. Sheng, A. Bhutani, D. J. Miller, D. P. Shoemaker, *J. Solid State Chem.* **2018**, *260*, 1.
[30] W. Bronger, U. Ruschewitz, P. Müller, *J. Alloys Compd.* **1995**, *218*, 22.
[31] X. W. Yan, M. Gao, Z. Y. Lu, T. Xiang, *Phys. Rev. Lett.* **2011**, *106*, 4.
[32] J. Zhao, H. Cao, E. Bourret-Courchesne, D. H. Lee, R. J. Birgeneau, *Phys. Rev. Lett.* **2012**, *109*, 267003.
[33] M. J. Benitez, O. Petracic, H. Tüysüz, F. Schüth, H. Zabel, *Phys. Rev. B* **2011**, *83*, 134424.
[34] M. Mézard, G. Parisi, N. Sourlas, G. Toulouse, M. Virasoro, *Phys. Rev. Lett.* **1984**, *52*, 1156.
[35] L. G. Wang, C. M. Zhu, D. L. G. C. Bao, Z. M. Tian, S. L. Yuan, *J. Mater. Sci.* **2015**, *50*, 5904.
[36] Y. Zhang, W. Rui, Z. Shi, S. Zhou, M. Yang, B. You, J. Du, *J. Supercond. Novel Magn.* **2016**, *29*, 531.
[37] M. Hudl, R. Mathieu, P. Nordblad, *Sci. Rep.* **2016**, *6*, 19964.
[38] P. Chen, J. Liu, H. Zhang, B. Chu, *IEEE Trans. Dielectr. Elect. Insul.* **2019**, *26*, 1716.
[39] W. B. Li, D. Zhou, L. X. Pang, R. Xu, H. H. Guo, *J. Mater. Chem. A* **2017**, *37*, 19607.
[40] D. Huang, W. L. Li, Z. F. Liu, Y. X. Li, C. Ton-That, J. Cheng, W. C. H. Choy, F. C. C. Ling, *J. Mater. Chem. A* **2020**, *8*, 4764.
[41] A. K. Bain, P. Chand, P. Ferroelectrics, *Principles and Applications, First Edition*, Wiley-VCH, Verlag GmbH, **2017**.
[42] X. Q. Song, W. Z. Lu, X. C. Wang, X. H. Wang, G. F. Fan, R. Muhammad, W. lei, *J. Eur. Ceram. Soc.* **2018**, *38*, 1529.
[43] M. Duchardt, U. Ruschewitz, S. Adams, S. Dehnen, B. Roling, *Angew. Chem., Int. Ed.* **2018**, *57*, 1351.
[44] A. R. West, *Solid State Chemistry and its Applications*, Wiley-VCH, Singapore, **2003**.
[45] A. Hayashi, N. Masuzawa, S. Yubuchi, F. Tsuji, C. Hotehama, A. Sakuda, M. Tatsumisago, *Nat. Commun.* **2019**, *10*, 5266.
[46] L. L. Wong, H. M. Chen, S. Adams, *Phys. Chem. Chem. Phys.* **2015**, *17*, 9186.
[47] D. Flak, A. Braun, A. Vollmer, *Sens. Actuators, B* **2013**, *187*, 347.
[48] G. Thiele, S. Lippert, F. Fahrnbauer, P. Bron, O. Oeckler, A. Rahimi-Iman, M. Koch, B. Roling, S. Dehnen, *Chem. Mater.* **2015**, *27*, 4114.
[49] G. Thiele, P. Bron, S. Lippert, F. Nietschke, O. Oeckler, M. Koch, B. Roling, S. Dehnen, *Inorg. Chem.* **2019**, *58*, 4052.
[50] W. Qarony, M. I. Hossain, M. K. Hossain, M. J. Uddin, A. Haque, A. R. Saad, Y. H. Tsang, *Results Phys.* **2017**, *7*, 4287.
[51] J. Androulakis, S. C. Peter, H. Li, C. D. Malliakas, J. A. Peters, Z. Liu, B. W. Wessels, J. -H. Song, H. Jin, A. J. Freeman, M. G. Kanatzidis, *Adv. Matter.* **2011**, *23*, 4163.
[52] J. Sun, A. Ruzsinszky, J. P. Perdew, *Phys. Rev. Lett.* **2015**, *115*, 036402.
[53] J. Sun, R. C. Remsing, Y. Zhang, Z. Sun, A. Ruzsinszky, H. Peng, Z. Yang, A. Paul, U. Waghmare, X. Wu, M. L. Klein, J. P. Perdow, *Nat. Chem.* **2016**, *8*, 831.
[54] R. Mittal, M. K. Gupta, S. L. Chaplot, M. Zbiri, S. Rols, H. Schober, Y. Sy, T.h. Brueckel, T. Wolf, *Phys. Rev. B* **2013**, *87*, 184502.

[55] I. R. Shein, A. L. Ivanovskii, *J. Supercond. Novel Magn.* **2011**, *24*, 2215.
[56] N. F. Mott, Z. Zinamon, *Rep. Prog. Phys.* **1970**, *33*, 881.
[57] A. Rohrbach, J. Hafner, G. Kresse, *J. Phys.: Condens. Matter* **2003**, *15*, 979.
[58] J. Varignon, M. Bibes, A. Zunger, *Phys. Rev. B* **2019**, *100*, 035119.
[59] M. Wang, M. Yi, H. Cao, C. de la Cruz, S. K. Mo, Q. Z. Huang, E. Bourret-Courchesne, P. Dai, D. H. Lee, Z. X. Shen, R. J. Birgeneau, *Phys. Rev. B* **2015**, *92*, 121101.
[60] R. Yu, J. X. Zhu, Q. Si, *Phys. Rev. Lett.* **2011**, *106*, 186401.